

# Design and Evaluation of a PMT High-Voltage system for Deepsea Neutrino Telescope

**Zhu Mao**<sup>1d</sup> **Shasha Liu**<sup>1a</sup> **Ruike Cao,**<sup>a</sup> **Hengbin Shao,**<sup>a</sup> **Yaowei Guo,**<sup>e</sup> **Sirui Wang,**<sup>d</sup> **Fuyudi Zhang,**<sup>a</sup> **Haoyan Zhang,**<sup>a</sup> **Tailin Zhu,**<sup>a</sup> **Yixi Jiang,**<sup>d</sup> **Hao Zhou,**<sup>a,b</sup> **Xin Xiang**<sup>a,b,c</sup> **Lei Wang**<sup>d</sup>

<sup>a</sup>*State Key Laboratory of Dark Matter Physics, Tsung-Dao Lee Institute & School of Physics and Astronomy, Shanghai Jiao Tong University, Shanghai 200240, China*

<sup>b</sup>*Key Laboratory for Particle Astrophysics and Cosmology (MOE) & Shanghai Key Laboratory for Particle Physics and Cosmology, Shanghai Jiao Tong University, Shanghai 200240, China*

<sup>c</sup>*Hainan Research Institute, Shanghai Jiao Tong University, Hainan 572024, China*

<sup>d</sup>*College of Nuclear Technology and Automation Engineering, Chengdu University of Technology, Chengdu, China*

<sup>e</sup>*Department of Physics, Imperial College of London, London United Kingdom*

**ABSTRACT:** We present the design and characterization of a Cockcroft–Walton (CW) high-voltage system developed for deep-sea neutrino telescopes. The system provides independently adjustable bias voltages to 31 three-inch PMTs inside a hybrid Digital Optical Module (hDOM). This paper describes the system design, control logic, test procedures, and the combined PMT–base performance, including baseline stability, gain uniformity, and timing accuracy. Performance was evaluated in the laboratory conditions that simulate the deep-sea environment. Baseline measurements indicate low and stable electronic noise, while gain calibration using single-photoelectron spectra shows that all PMTs can be tuned to a common nominal gain and remain stable over multi-day operation. Transit-time-spread measurements yield values below 1.8 ns (FWHM), consistent with manufacturer specifications. These results demonstrate that the CW-based system delivers the stability and timing precision required for deep-sea multi-PMT optical modules.

**KEYWORDS:** PMT, Cockcroft-Walton HV System, Neutrino Telescope

**ARXIV EPRINT:** [1234.56789](https://arxiv.org/abs/2512.14382)

---

<sup>\*</sup>These authors contributed equally to this work.

<sup>†</sup>Corresponding authors. Email: [xxiang@sjtu.edu.cn](mailto:xxiang@sjtu.edu.cn), [lw@cdut.edu.cn](mailto:lw@cdut.edu.cn)

---

## Contents

<b>1</b>	<b>Introduction</b>	<b>1</b>
<b>2</b>	<b>The PMT HV System</b>	<b>2</b>
2.1	Overall Design	2
2.2	Base and Control Board Implementation	3
2.3	Base High Voltage Test	5
2.4	Control Logic	6
<b>3</b>	<b>PMT Performance</b>	<b>7</b>
3.1	Experimental Setup	7
3.2	PMT gain measurement and stability	9
3.3	PMT Time Resolution	12
<b>4</b>	<b>Summary and Discussion</b>	<b>13</b>

---

## 1 Introduction

Neutrino telescopes detect high-energy neutrinos from astrophysical sources such as active galactic nuclei and core-collapse supernovae, providing probes of cosmic accelerators, multi-messenger phenomena, and fundamental physics beyond the Standard Model [1–3]. These instruments rely on the detection of Cherenkov photons produced by charged particles generated in neutrino interactions within transparent media such as seawater or ice. Photomultiplier tubes (PMTs) serve as the primary optical sensors, converting photon signals into electrical pulses, whose timing and charge encode the event topology and energy. Because the detectors are deployed at great depths or embedded in ice, the PMTs and their front-end electronics must operate reliably inside sealed, pressure-resistant glass vessels that preserve optical clarity and mechanical integrity. Stable and well-regulated high voltage is essential, as it directly determines the PMT gain and timing response, which in turn impacts photon hit resolution, and ultimately the quality of neutrino reconstruction. Therefore, the design of the PMT housing, its high-voltage, and readout systems plays a critical role in the overall sensitivity and long-term performance of the telescope.

The TRIDENT (TRopical DEep-sea Neutrino Telescope) neutrino telescope deploys an array of hybrid Digital Optical Modules (hDOMs) anchored at depths exceeding 3,000 m [4]. Each hDOM integrates two complementary photon-sensing technologies—31 three-inch PMTs and 24 silicon photomultipliers (SiPMs)—to achieve high photo-coverage and directional sensitivity [5, 6]. This hybrid approach follows the multi-PMT DOM concept pioneered in KM3NeT [7]. The sensors are housed within a 17-inch-diameter borosilicate glass vessel, manufactured by Nautilus, with a 14 mm wall thickness, providing over 95 % optical transparency and sufficient mechanical strength to withstand pressures up to 670 bar [8]. An aluminum support frame holds all sensors in fixed

orientations, while the volume between the frame and the inner wall of the glass vessel is filled with high-transparency optical gel that ensures stable optical coupling.

The compact integration of multiple sensors within the 17-inch vessel imposes stringent requirements on system stability and control. Because recovery or maintenance at kilometer-scale depths is costly and technically demanding, each hDOM must operate reliably for long periods without intervention. The high-voltage (HV) system is a critical component, as its stability directly determines the PMT gain and signal-to-noise ratio, which in turn affect the detection of faint Cherenkov photons and the accuracy of event reconstruction. To meet these requirements, a CW voltage multiplier is adopted for its compact and efficient design. Its ability to generate high voltages with a minimal number of components makes it particularly suitable for the confined geometry of deep-sea optical modules [9].

This paper presents the design and performance evaluation of a CW based high-voltage system developed for deep-sea neutrino telescope applications [10]. The system architecture is described with an emphasis on achieving low output ripple and long-term voltage stability. Performance is validated through circuit simulations and laboratory measurements. Sec. 2 outlines the CW circuit design, control logic, and test procedures. Sec. 3 reports the PMT response, including baseline ripple and gain stability under simulated deep-sea conditions. Sec. 4 summarizes the results and discusses their relevance to future large-scale neutrino detectors.

## 2 The PMT HV System

### 2.1 Overall Design

The HV system adopts a distributed architecture in which each PMT is equipped with its own Cockcroft–Walton (CW) module, enabling independently adjustable bias voltages for all 31 channels in an hDOM. This one-CW-per-PMT scheme ensures uniform gain tuning, isolates channel-level variations, and avoids single-point failure modes. A dedicated control board provides channel selection and command fan-out, while the hDOM motherboard FPGA [11] issues commands through a shared communication interface. This three-tier structure – motherboard FPGA, control board, and per-PMT CW bases – offers scalable and robust HV control. Each CW base has a compact 47 mm × 47 mm footprint, allowing all 31 modules to fit within the tight mechanical envelope of deep-sea optical modules [12].

Fig. 1 shows a representative assembly of the system. The control board connects to the FPGA motherboard via a 14-pin connector and manages communication with all 31 base boards through an I<sup>2</sup>C hub. The FPGA motherboard is responsible for digitizing and processing PMT signals and communicates with the control board over the I<sup>2</sup>C interface to monitor and adjust the bias voltage. The control board distributes power and commands via the I<sup>2</sup>C hub, enabling independent channel control and simplifying the layout of the motherboard. Each base features a CW voltage multiplier circuit to generate the PMT bias voltage, an integrated ADC to monitor the output, and return voltage data to the control board for closed-loop regulation. This work focuses on the design and development of the control board and the PMT base boards. The FPGA motherboard was also designed and developed by the TRIDENT collaboration, but will not be discussed in detail here.

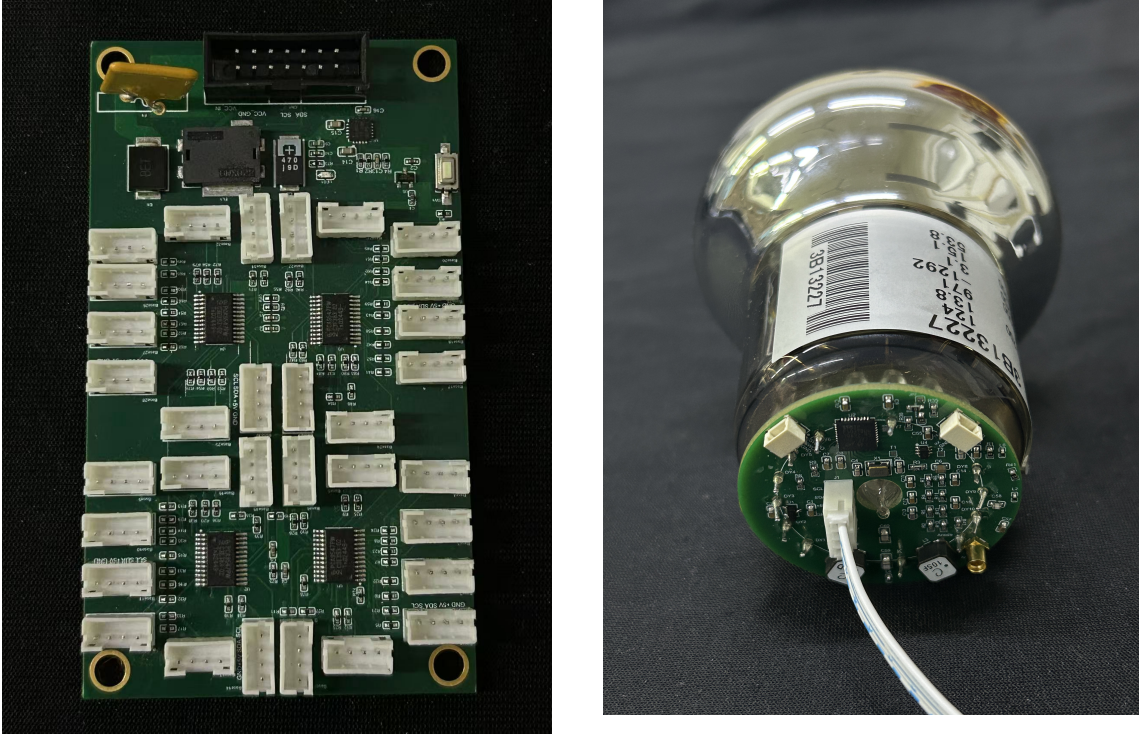


**Figure 1.** Photo of the PMT high-voltage system, consisting of (left) the control board and (right) the PMT-integrated base board

## 2.2 Base and Control Board Implementation

The control board manages voltage configuration and communication for all 31 bases through a multiplexed I<sup>2</sup>C architecture. The control board is connected to the FPGA motherboard via a 14-pin header, which also interfaces with four 8-channel I<sup>2</sup>C-bus multiplexers with a reset (PCA9547). As shown in Fig. 2, each PCA9547 is routed to eight Base connectors. Upon power-up, the PCA9547 enables Channel 0 by default. Therefore, to avoid I<sup>2</sup>C bus contention, Channel 0 on the remaining three devices is disabled before communication begins. Using the PCA9547 eliminates the need to assign 31 unique device addresses and simplifies firmware configuration. During operation, enabling one PCA9547 channel at a time selects the corresponding Base for I<sup>2</sup>C communication. Tests confirm that the FPGA motherboard can address and monitor all 31 Bases via I<sup>2</sup>C without conflict.

Voltage monitoring and control signals are transmitted back to the FPGA motherboard via the same multiplexed I<sup>2</sup>C network. After being scaled down by a precision resistor divider, the high voltage signal is sampled by an ADC. The MCU samples the high-voltage output using the on-board ADC and transmits the measurements to the control board over the I<sup>2</sup>C bus. The control board includes power-protection circuitry and four 8-channel I<sup>2</sup>C multiplexers with reset capability. Because each device powers up with Channel 0 enabled by default, the FPGA first disables all channels to avoid bus contention. A selected channel is then enabled to establish communication with the corresponding Base, allowing voltage configuration and readback through the FPGA motherboard.

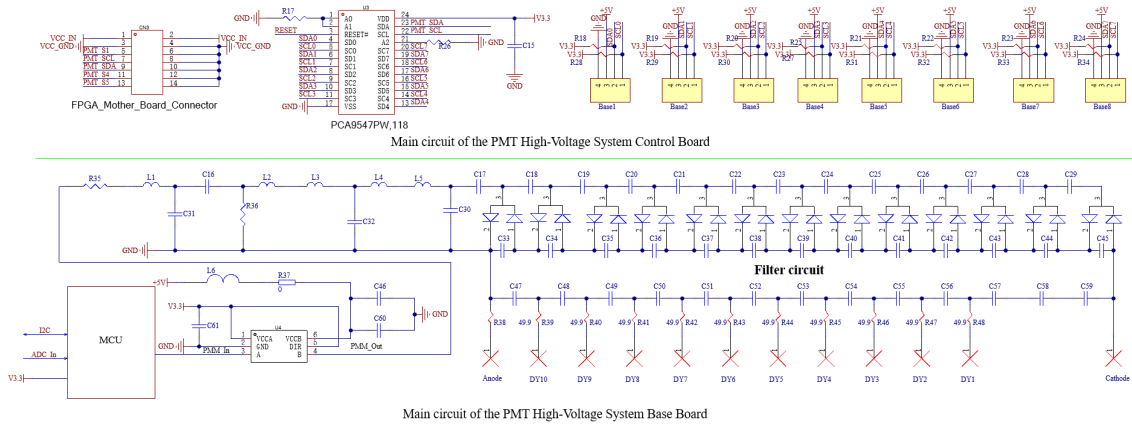


**Figure 2.** Main circuit of the PMT high-voltage system

Each PMT base consists of three functional blocks: an MCU, an inductive resonant driver, and a CW voltage multiplier, as shown in Fig. 2. The inductive resonant circuit is dominated by the inductors L3 and L5. The CW circuit is primarily composed of multiple diodes and capacitors. The MCU generates a pulse-width-modulated (PWM) signal whose frequency and duty cycle control the drive amplitude. Through a USB-to-serial interface, the output voltage is adjustable from 0 V to -1.5 kV, and real-time feedback from the on-board ADC provides closed-loop regulation. The resonant driver converts the DC supply into an AC waveform, while low-/high-pass filters and ferrite beads suppress switching noise[13][14].

The CW multiplier and resonant driver form the core of the high-voltage generation circuit on the base. The multiplier is built from cascaded diode–capacitor stages implementing a 3:1:1:1:1:1:1:1:1:1 dynode voltage ratio, as recommended for the Hamamatsu R14374 and NNVT N2031 PMT to reduce transition-time spread and maintain timing uniformity. A PWM waveform generated by the MCU passes through low-pass and high-pass filters to suppress switching noise before driving the LC resonant stage. Depending on the resonant parameters, the PWM frequency is set to approximately 80 kHz, producing a 100–150 V<sub>pp</sub> AC signal that feeds the multiplier. A parallel RC filter smooths the rectified output to provide a stable DC bias for PMT operation. The bases operate inside a sealed 0.5–0.7 atm nitrogen environment within the glass sphere, where the seawater temperature remains 2–4 °C. Under these conditions, the design should produce stable high-voltage outputs with sub-millivolt baseline fluctuations.

The operation of the CW multiplier can be understood by analyzing the two phases of the input AC waveform (typically  $\sim 80$  kHz). During the positive half-cycle, the input polarity forward-biases a set of diodes, allowing the upper-tier capacitors (C33,C34,C35) to charge. Each capacitor charges to a voltage close to the peak value of the input AC source ( $V_{pp}$ ). During the negative half-cycle, the input polarity reverses. The previously charged upper-tier capacitors act as series voltage sources, adding to the input drive. This combined voltage forward-biases the next diode stage and charges the lower-tier capacitors (C17, C18, C19). The resulting voltage on these capacitors approaches  $2V_{pp}$  in the first stage, with the multiplication effect propagating through subsequent stages.

A key advantage of the CW topology is that the voltage stress on each capacitor does not

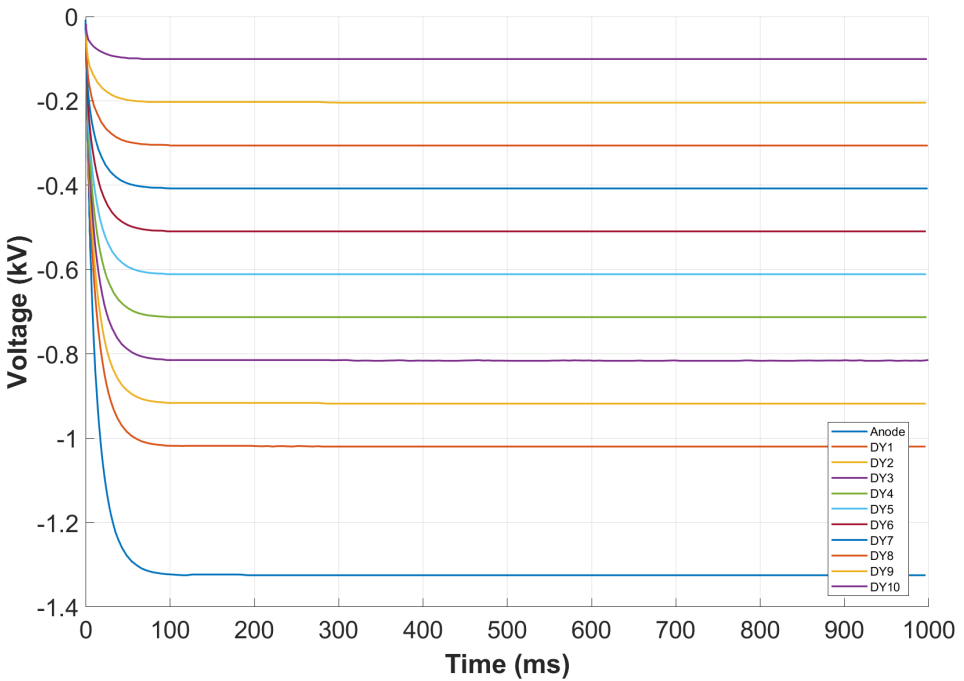


**Figure 3.** Simulated high-voltage time evolution at different stages of the CW multiplier. All stages converge to their steady-state values with uniform voltage spacing along the multiplication chain.

exceed  $2 V_{pp}$ , permitting the use of capacitors with lower voltage ratings than the overall output. The high-voltage output is then routed through a filter network and series damping resistors. These resistors suppress overshoot and high-frequency ringing caused by the PMT’s output capacitance, improving pulse stability. The polarity of the output is determined by the diode orientation; for example, a positive high voltage for the PMT cathode is obtained by reversing the diode directions relative to a negative-output configuration.

### 2.3 Base High Voltage Test

We simulated the performance of the CW base to evaluate voltage buildup and steady-state behavior across the multiplier stages. The circuit was modeled in ADI LTspice using component values that match those of the prototype, including the resistor–capacitor network and output filter. Fig. 3 shows the simulated stage voltages as a function of time. All stages reach their steady-state values after roughly 100 ms, with uniform voltage spacing along the multiplication chain that is consistent with the design specifications.

**Table 1.** Electrode Voltages of the PMT Base Board (V)

Electrodes	P	Dy10	Dy9	Dy8	Dy7	Dy6	Dy5	Dy4	Dy3	Dy2	Dy1	K
$V_{Base1}$	0	-104	-208	-311	-412	-513	-615	-706	-805	-900	-998	-1274
$V_{Base2}$	0	-104	-208	-312	-415	-515	-613	-711	-806	-902	-997	-1270
$V_{Base3}$	0	-104	-209	-312	-414	-515	-613	-711	-806	-900	-995	-1266
$V_{sim}$	0	-104	-208	-312	-416	-520	-624	-724	-832	-936	-1040	-1352

Three bases were tested to verify the dynode voltages and their consistency with the designed ratio. Each unit was placed on an insulating substrate to avoid external interference. Stage voltages from DY10 to the cathode were measured sequentially using a high-voltage probe (HVP-40, 1000:1 attenuation), with readings taken after a 5-second stabilization period. The first base yielded  $-104$  V at DY10, which was adopted as the reference setting for the remaining units. During all measurements, the anode (P) was held at ground, and the cathode (K) reached approximately  $-1270$  V. Table 1 lists the measured stage voltages, which follow the expected CW scaling and agree with the LTspice simulation. Under the conditions of a regulated 5 V input and a  $-1200$  V output, the comprehensive performance of the base board was evaluated, with the key results summarized in Table 2.

**Table 2.** Specifications of the High-Voltage Base board

Parameter	Value
Input Voltage	5 V
Output Voltage Range	$-1500$ V to 0 V
Ripple (Anode to GND)	$\sim 150$ mV <sub>pp</sub>
Power Consumption (Switch-on)	$< 60$ mW (at $-1200$ V)
Settling Time	$\sim 3$ s
Output Stability	0.1% (under stable input)

## 2.4 Control Logic

The PMTs operate at a typical  $-1250$  V to achieve a gain of  $10^7$ . Because the gain follows a power-law dependence on the bias voltage, small variations in bias can lead to significant deviations in gain. The HV required for a specific PMT varies due to differences in the manufacturing processes of Hamamatsu and NNVT. To achieve a uniform response across the array, each of the 31 PMTs within an hDOM requires individually adjustable HV control. Furthermore, the gain may drift over extended periods of operation, and specific channels may need to be selectively disabled under deep-sea conditions. These considerations necessitate fine, stable, and independently configurable high-voltage control for all PMTs.

Each base MCU is programmed with a default PWM frequency (typically 80 kHz) and a 50% duty cycle, which produces an initial high-voltage output. Regulation is achieved by comparing the on-board ADC reading with the target value. Adjusting the PWM frequency provides coarse

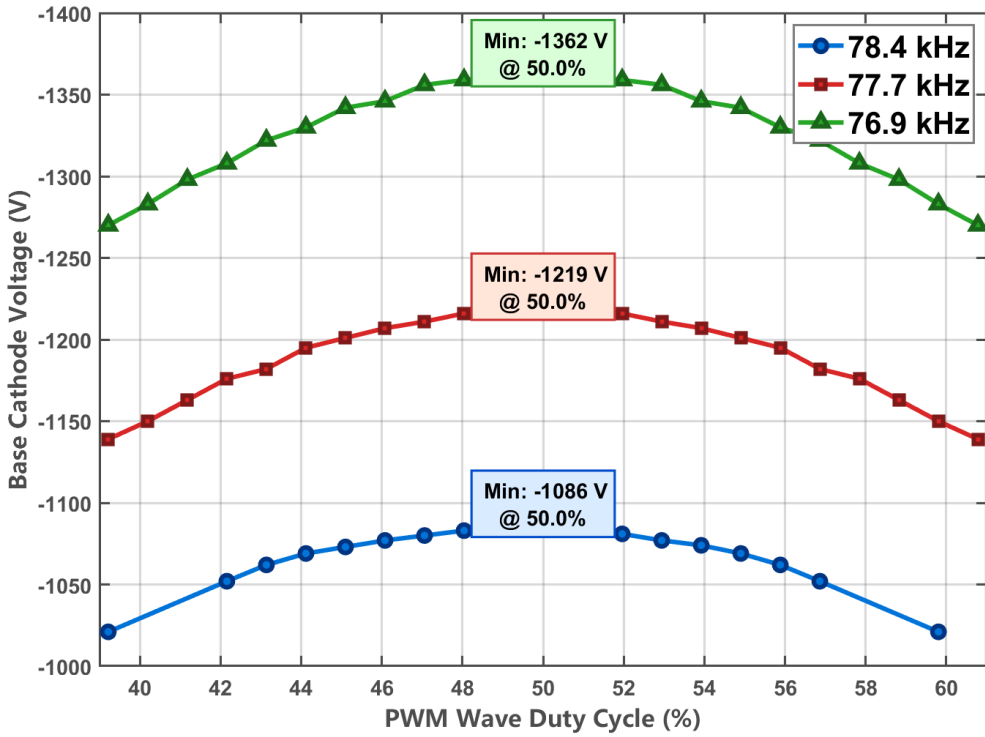


**Figure 4.** Cathode voltage as a function of the duty cycle at different driving frequencies

control, with each step corresponding to roughly a 100 V change in output voltage. Fig. 4 shows the relationship between the PWM parameters and the cathode voltage: the output peaks near a 50% duty cycle and decreases symmetrically toward either end in a near-parabolic profile.

After system integration, the FPGA executes a two-step control sequence. FPGA first scans the PWM drive frequency around an initial reference to reach the approximate target range, and then iteratively fine-tunes the duty cycle based on feedback from the on-board ADC until the desired high-voltage value is achieved. This closed-loop procedure enables each PMT base to autonomously converge to its operating voltage with sub-percent precision, ensuring uniform gain calibration and stable performance across all channels.

### 3 PMT Performance

#### 3.1 Experimental Setup

The objective of this study is to evaluate the performance and stability of PMTs equipped with soldered CW bases. Measurements focus on baseline stability, gain, and time resolution, as well as assessing environmental influences, such as temperature.

All measurements are performed in a dark room to maintain a stable optical environment. To measure the timing performance, a PMT test bench equipped with a picosecond laser is adopted, as shown in Fig. 5. A picosecond laser emitting at 532 nm served as the pulsed light source.

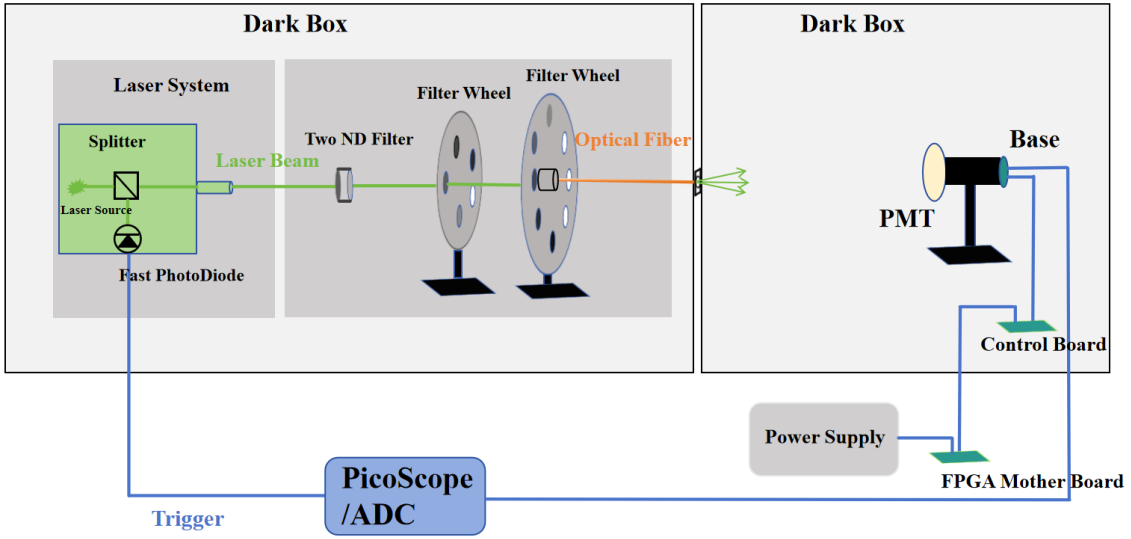


**Figure 5.** The PMT bench test setup designed for SPE gain, gain curve and time resolution measurements with main components marked.

Component	OD	Transmission
<b>Two ND Filters</b>	1	10%
	4	0.01%
<b>Five-position Filter Wheel</b>	0.2	63.1%
	0.4	39.8%
	0.6	25.1%
	0.9	12.6%
	Empty	1
<b>Eight-position Filter Wheel</b>	1	10%
	2	1%
	3	0.1%
	4	0.01%
	Empty	1
	Slots 6–8: Black	0

**Table 3.** Optical densities (OD) of all neutral density (ND) filters used in the setup. By combining these filters, the total attenuation can span a wide range, up to  $7.94 \times 10^9$ . Note that "black" positions correspond to nearly zero transmission.

The laser delivered pulses with a temporal width of about 10 ps, pulse energies exceeding 1  $\mu$ J, and a repetition rate adjustable from 500 Hz to 300 kHz. The laser output was split by an optical splitter: one branch illuminated the PMT, while the other was sent to a fast photodiode that provided a reference trigger for the oscilloscope. The illumination beam passed sequentially through two optical attenuators and two motorized ZWO 1.25-inch filter wheels loaded with neutral-density filters of various attenuation factors. Table 3 summarizes all parameters and specifications of the ND filters used in the setup. The attenuated beam was then coupled into an optical fiber

and directed onto the PMT through a diffuser fiber tip. Both the laser and the filter wheels were remotely controlled to vary the light intensity over a wide dynamic range. Data acquisition was performed using a PicoScope 6426E oscilloscope [15].

For stability and environmental tests, in this work, we will show results from our tests on 31 PMTs in one hDOM. The 31 PMTs and the complete HV system were integrated into an hDOM and placed in a temperature-controlled chamber maintained at 2°C. The internal volume of the hDOM was filled with nitrogen gas at a pressure of  $\sim 0.5$  atm, replicating the thermal and pressure conditions expected during deep-sea operation. Gain and baseline stability were evaluated by monitoring single-photon dark-count signals under these conditions.

### 3.2 PMT gain measurement and stability

The PMT gain was calibrated using single-photoelectron (SPE) charge spectra measured under low-light conditions, where the mean photoelectron occupancy satisfies  $\lambda \ll 1$ . The charge of each PMT pulse is obtained by integrating the waveform over a predefined time window around the pulse. The resulting charge distribution,  $f(q)$ , can be modeled as a Poisson-weighted sum of  $n$ -photoelectron contributions [16]:

$$f(q) = B \left( \text{Poisson}(0; \lambda) \text{Ped}(q) + \sum_{n=1}^{\infty} \text{Poisson}(n; \lambda) (\text{Ped} \otimes \underbrace{\text{SPE} \otimes \cdots \otimes \text{SPE}}_{n \text{ times}})(q) \right). \quad (3.1)$$

Here,  $\text{Ped}(q)$  denotes the Gaussian electronic pedestal,  $B$  is the normalization factor, and  $\lambda$  is the mean detected photoelectron count. The SPE response function is parameterized following Ref. [16] as a sum of two Gamma components and an exponential low-charge tail,

$$\text{SPE}(q) = \eta_1 \Gamma(q; \mu, b) + \eta_2 \Gamma(q; \mu f_{\mu}, b f_b) + \begin{cases} \eta_3 \ell e^{-\ell q}, & q < \mu, \\ 0, & q > \mu, \end{cases} \quad (3.2)$$

where the first Gamma term describes full dynode multiplication [17], the second captures reduced-charge events from incomplete multiplication at early dynodes, and the exponential term models the continuous low-charge population arising from elastic backscattering and other partial-amplification processes. This gamma family has been shown to reproduce the full SPE lineshape in many cases [16, 18, 19].

A binned  $\chi^2$  minimization was used to extract the ten free parameters governing the pedestal, SPE response, and Poisson occupancy. An example fitted charge spectrum is shown in Fig. 6. The gain uncertainty is obtained by propagating the parameter covariance from the SPE-spectrum fit to the mean SPE charge. This provides the statistical error on the extracted gain.

The dependence of gain on the bias voltage is well described by a power-law model,

$$G(V) = \alpha V^{\beta}, \quad (3.3)$$

where  $\beta$  characterizes the voltage sensitivity of the amplification. To determine the parameters  $\alpha$  and  $\beta$ , the gain was measured at several high-voltage settings between  $-1100$  V and  $-1300$  V. The resulting gain–voltage relation is shown in Fig. 6. Because the gain–voltage response varies from

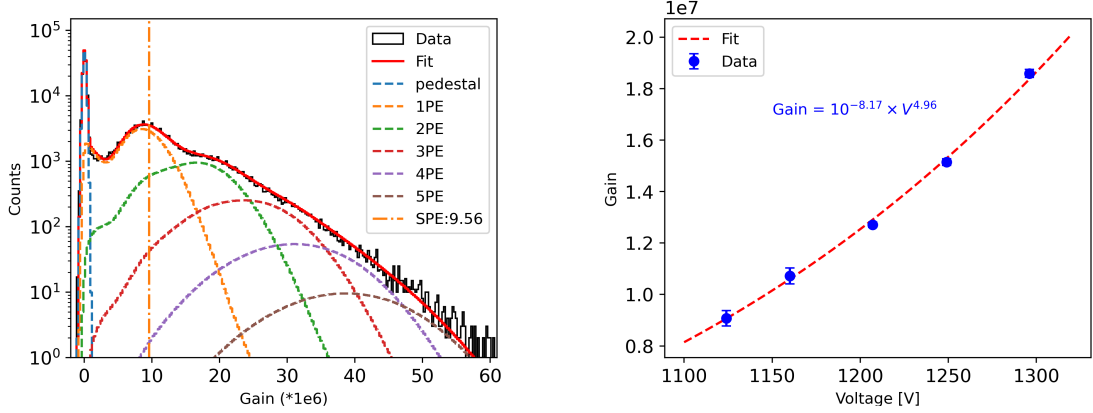


**Figure 6.** Left: The charge spectrum and the fit function. The measurement was performed with the experimental setup presented in Fig.5. Right: SPE gain curve as a function of bias voltage. The points correspond to the mean charge of the 1-PE peak obtained from the fits in the left panel.

PMT to PMT, measuring the gain curve for each unit allows the bias voltage to be tuned later to restore the target gain as the tube ages or its response drifts.

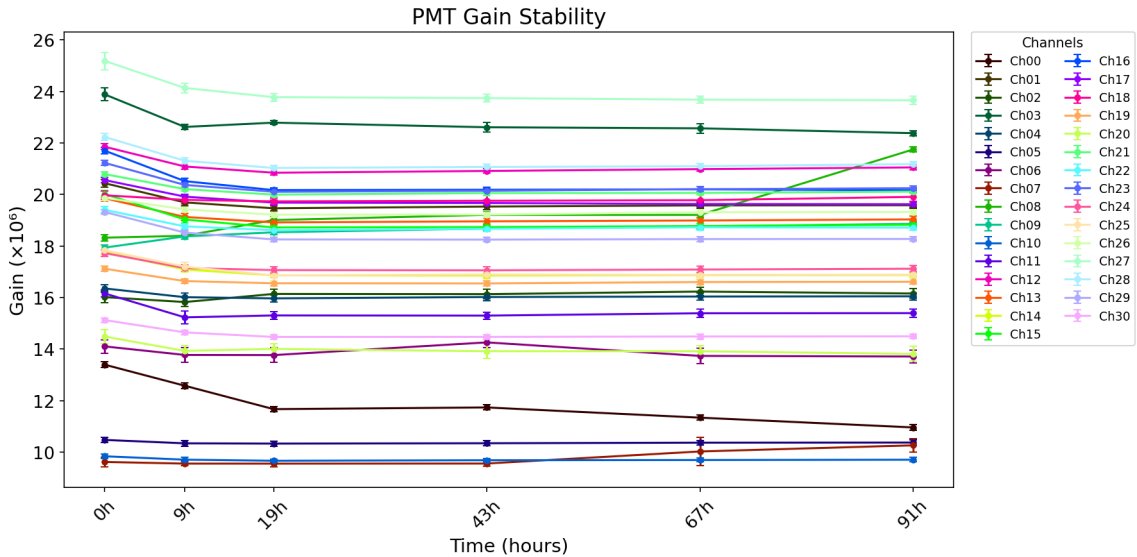


**Figure 7.** Gain stability of the 31 PMTs in the hDOM as a function of time. Each data point represents the mean gain over a 5-hour run, where the error bars indicate the the covariance of the spe gain fit. The first run is defined as 0 h, and subsequent runs correspond to 9 h, 19 h, 43 h, 67 h, and 91 h, respectively. The gains stabilize after approximately 20 hours, with most PMTs fluctuating within  $\pm 2 - 3\%$  of their initial values.

After completing the base soldering procedure and assembling 31 PMTs into a single hDOM, the hDOM was continuously powered and operated for around 100 hours at a fixed high voltage (corresponding to a gain of  $1 \times 10^7$ ), in order to assess their long-term gain and baseline stability. Throughout this period, six data runs, each covering around 5 hours, were recorded using the moth-

erboard designed for TRIDENT Phase-I [20], which features a 125 MSps ADC. After determining the gain–voltage parameters, the bias of each PMT was set to achieve a uniform nominal gain. The long-term gain stability of the 31 PMTs in the hDOM was then evaluated using the dark-count data. Each recorded waveform spans 480 ns (60 ADC samples). The first run defines  $t = 0$  h, and the subsequent runs were taken at 9, 19, 43, 67, and 91 h. For each run, the plotted value represents the mean gain over the full 5-hour dataset, and the error bars indicate the covariance of the spe gain fit. Fig. 7 shows the gain evolution over time. The gains stabilize after approximately 20 hours of continuous operation. For most channels, the variation remains within  $\pm 2$ –3% of the initial value, and no systematic drift or monotonic trend is observed. Even the PMTs with the highest initial gains remain stable to within 5% throughout the measurement period. For the baseline stability of PMTs, the standard deviation of the first 20 samples was used to quantify the baseline fluctuation for each waveform. Fig. 8 shows the resulting stability over time. The run schedule is identical to that used for the gain measurement. For each run, the plotted value represents the mean baseline fluctuation over the full 5-hour dataset, and the error bars indicate the variation within that period.

The baseline stabilizes after roughly 40 hours of continuous operation, with channel-to-channel variations within 2%. This indicates negligible drift in the front-end electronic noise. Because baseline fluctuation directly affects the signal-to-noise ratio and effectively determines the single photoelectron (SPE) trigger threshold, these results demonstrate that the readout system maintains consistently low-noise performance suitable for long-duration deep-sea operations.

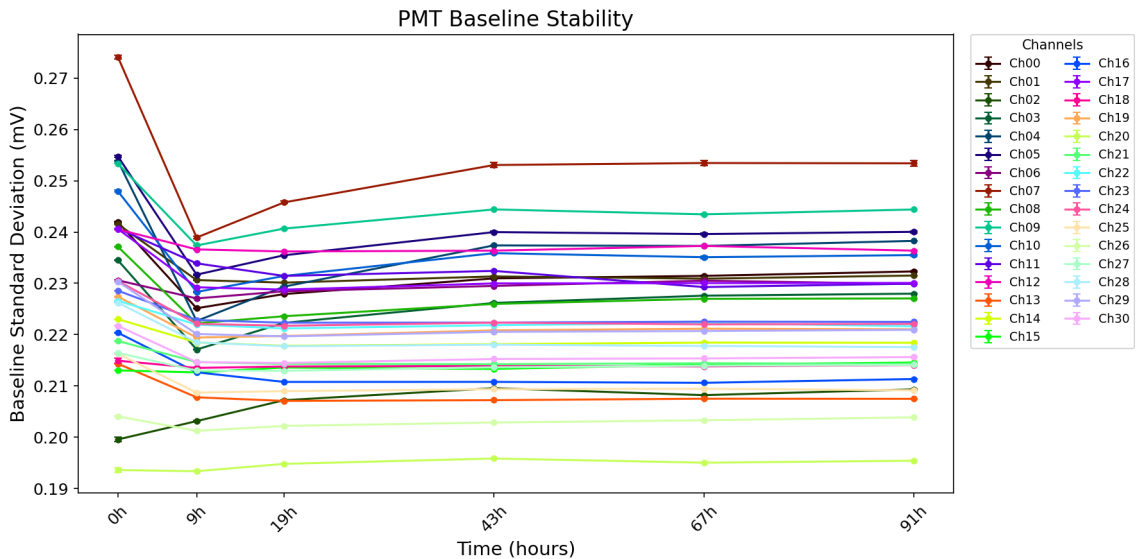


**Figure 8.** Baseline fluctuation of 31 PMT channels as a function of operation time. The baseline values were derived from the dataset described in Fig. 7, each data point represents the mean baseline fluctuation over a 5-hour run, where the error bars indicating the standard deviation within that period. The results show that the baseline stabilizes after about 40 hours of continuous operation, with channel-to-channel variations constrained within 2%, demonstrating negligible drift in front-end electronic noise.

### 3.3 PMT Time Resolution

Precise photon timing is essential for neutrino telescopes, as the reconstruction of tracks and cascade directions and vertices relies on the arrival times of Cherenkov photons at optical modules. Simulation has shown that sub-degree angular resolution for muon tracks can be achieved only if the per-photon timing precision is on the order of 2 ns [21]. This requirement arises primarily from the intrinsic transit-time spread (TTS) of the PMT, the chromatic dispersion in seawater, and the undersea acoustic positioning accuracy. The PMT TTS, defined as the full width at half maximum (FWHM) of the distribution of single photoelectron (PE) transit times, is a key detector parameter to be evaluated.

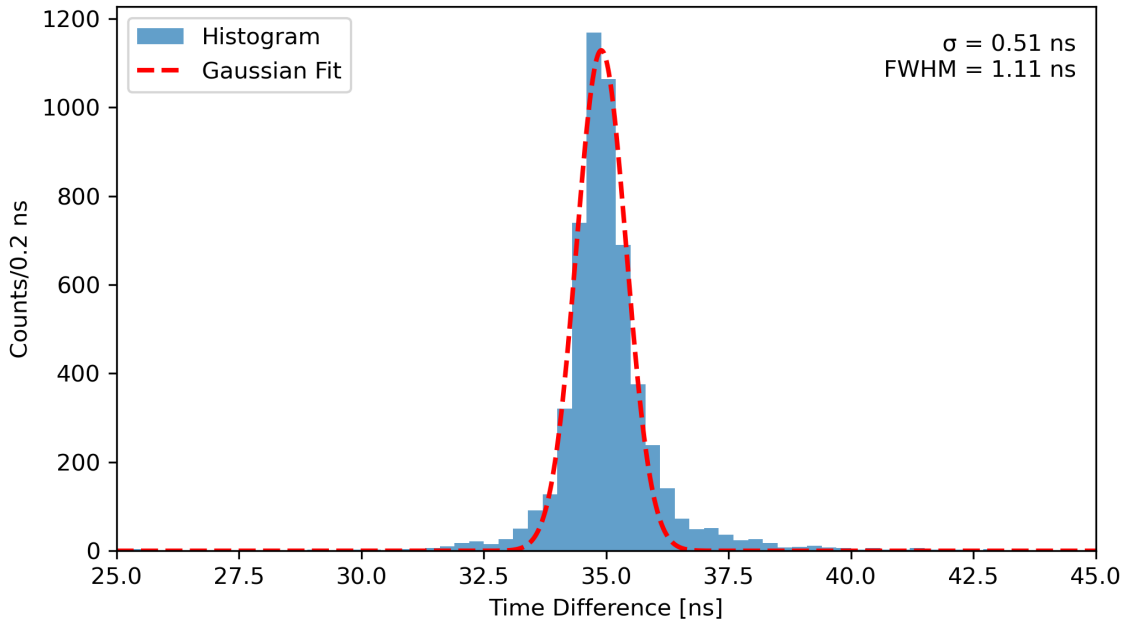


**Figure 9.** Transit Time Spread (TTS) measurement at a PMT gain of  $10^7$ . The histogram shows the distribution of the time difference between the laser trigger and the PMT response, and the red dashed line shows the Gaussian fit applied to the prompt peak. The FWHM extracted from the distribution is 1.11 ns.

The TTS of each PMT is measured using the setup shown in Fig. 5. The laser intensity is adjusted to maintain a single-PE occupancy of approximately 0.05. PMT waveforms are digitized using the PicoScope sampling at 5 GSps. The laser system includes an internal optical splitter and a fast photodiode. An emitted laser pulse is divided into two paths: one eventually hits the PMT and the other hits the photodiode, which generates a reference electrical signal. The timing jitter of this reference channel, calibrated by the manufacturer, is less than 20 ps. This configuration allows sub-ns accuracy in the TTS measurement.

The photon arrival time on a PMT is defined as the point where the PMT waveform exceeds one third of SPE amplitude. For each event, the transit time (TT) is calculated as the time difference between the PMT signal and the reference laser trigger. A fixed offset caused by unequal propagation paths of the optical pulse and electrical reference signal was measured independently using a silicon photomultiplier (SiPM, S PTR  $\sim$ 150 ps) [22] and is subtracted from PMT signals. A representative

TTS measurement is shown in Fig. 9. The TTS is typically extracted either from the width of the Gaussian core or directly from the full distribution. As expected for small-mass PMTs, the distribution shows a mild asymmetry with a late-time tail arising from delayed electron trajectories, including elastic back-scattering at the first dynode.

The Hamamatsu PMTs are specified to have a TTS below 1.8 ns (FWHM). This value was verified by the manufacturer using a conventional resistive-divider base during quality assurance tests. The measurements obtained with the CW-base configuration are consistent with these specifications, confirming that the CW design preserves the intrinsic timing performance required for deep-sea neutrino telescope applications.

## 4 Summary and Discussion

This work presents the design, implementation, and validation of a Cockcroft–Walton–based high-voltage system developed for deep-sea neutrino telescopes. The system integrates an FPGA-controlled PWM driver, an LC resonant stage, and a multi-stage CW multiplier to provide independently adjustable, low-noise bias voltages for 31 PMTs within an hDOM. Laboratory tests demonstrate stable voltage regulation, accurate gain tuning, and reliable time performance over extended operation.

Baseline measurements show that all 31 PMTs maintain fluctuations at the 0.3%–1.4% level over five days, confirming the low-noise behavior of the front-end electronics. The CW-base configuration achieves a transit-time spread below 1.8 ns (FWHM), consistent with manufacturer specifications and sufficient for photon-timing requirements in deep-sea reconstruction. Gain measurements indicate that each PMT can be tuned to a common nominal gain, and the gain remains stable to within a few percent over the multi-day test period.

These results confirm that the system achieves the voltage stability, timing performance, and gain uniformity required for a deep-sea optical module, and is suitable for scaling to larger multi-PMT detectors in long-term deployments.

## Acknowledgments

This work is supported by the Ministry of Science and Technology of China under National key research and development plan (Grant no. 2023YFC3107402). X. Xiang would like to thank the Double First-Class startup funds provided by Shanghai Jiao Tong University.

## References

- [1] T.K. Gaisser, R. Engel and E. Resconi, *Cosmic Rays and Particle Physics*, Cambridge University Press, 2nd ed. (2016).
- [2] F. Halzen and S.R. Klein, *IceCube: An Instrument for Neutrino Astronomy*, *Rev. Sci. Instrum.* **81** (2010) 081101 [[1007.1247](#)].
- [3] S.A.-M. et al. [KM3NeT Collaboration], *Letter of intent for km3net 2.0*, *J. Phys. G* **43** (2016) 084001.
- [4] TRIDENT collaboration, *A multi-cubic-kilometre neutrino telescope in the western Pacific Ocean*, *Nature Astron.* **7** (2023) 1497 [[2207.04519](#)].

- [5] W. Zhi, J. Zheng, W. Tian, D. Xu and X. Xiang, *Preliminary Design of the Hybrid Digital Optical Module for TRIDENT*, *PoS ICRC2023* (2023) 1213.
- [6] H. Shao et al., *A cost effective optimization of the hybrid-dom design for trident*, [2507.10256](#).
- [7] P.K. et al. [KM3NeT Collaboration], *The km3net digital optical module and its electronics*, *JINST* **14** (2019) P03021.
- [8] N.M.S. GmbH, *VITROVEX 17-inch glass spheres (technical data sheet)*, 2017.
- [9] R.A. et al. [IceCube Collaboration], *The design and performance of icecube doms*, *Nucl. Instrum. Meth. A* **618** (2010) 139.
- [10] J.D. Cockcroft and E.T.S. Walton, *Experiments with high velocity positive ions. I. further developments in the method of obtaining high velocity positive ions*, *Proceedings of the Royal Society A* **136** (1932) 619.
- [11] G. Zhang, Y. Yang and D. Xu, *A waveform and time digitization mainboard prototype for the hybrid digital optical module of TRIDENT neutrino experiment*, [2507.00548](#).
- [12] P. Kooijman, S. Adrián-Martínez, M. Ageron et al., *The km3net digital optical module and its electronics*, *Journal of Instrumentation* **14** (2019) P03021.
- [13] P. Timmer, E. Heine and H. Peek, *Very low power, high voltage base for a photo multiplier tube for the km3net deep sea neutrino telescope*, *Journal of Instrumentation* **5** (2010) C12049.
- [14] The IceCube Collaboration, *Design and performance of the multi-PMT optical module for IceCube Upgrade*, in *Proceedings of the 37th International Cosmic Ray Conference (ICRC 2021)*, vol. 395 of *PoS*, p. 1070, Sissa Medialab, 2021, [DOI](#).
- [15] Pico Technology, *Picoscope 6000e series oscilloscopes: Data sheet*, 2024.
- [16] DEAP collaboration, *In-situ characterization of the Hamamatsu R5912-HQE photomultiplier tubes used in the DEAP-3600 experiment*, *Nucl. Instrum. Meth. A* **922** (2019) 373 [[1705.10183](#)].
- [17] J. Prescott, *A statistical model for photomultiplier single-electron statistics*, *Nuclear Instruments and Methods* **39** (1966) 173.
- [18] M. Akashi-Ronquest et al., *Triplet Lifetime in Gaseous Argon*, *Eur. Phys. J. A* **55** (2019) 176 [[1903.06706](#)].
- [19] L.N. Kalousis, J.P.A.M. de André, E. Baussan and M. Dracos, *A fast numerical method for photomultiplier tube calibration*, *JINST* **15** (2020) P03023 [[1911.06220](#)].
- [20] G. Zhang and Y. Yang, *Design and Performance of the hDOM Motherboard for TRIDENT Phase-I*, *PoS ICRC2025* (2025) 591.
- [21] J.A.A. et al., *Time calibration of the antares neutrino telescope*, *Astropart. Phys.* **34** (2011) 539.
- [22] W. Zhi, R. Cao, J. Tang, M. Wang, Y. Tan, W. Wu et al., *Front-end electronics development of large-area SiPM arrays for high-precision single-photon time measurement*, *JINST* **19** (2024) P06011 [[2403.02948](#)].